Implantation Length and Thermal Stability of Interstitial Ar Atoms in Boron Nitride Nanotents

Huanyao Cun,[†] Marcella Iannuzzi,[‡] Adrian Hemmi,[†] Jürg Osterwalder,[†] and Thomas Greber[†,*]

[†]Physik-Institut and [‡]Physikalisch-Chemisches Institut, Universität Zürich, Winterthurerstrasse 190, CH-8057 Zürich, Switzerland

ABSTRACT Hyperthermal atoms may be implanted beneath single layers of graphene or hexagonal boron nitride (*h*-BN) on a substrate. For the case of *h*-BN on rhodium, which is a corrugated honeycomb superstructure with a periodicity of 3.2 nm, Ar atoms are implanted at distinct interstitial sites within the supercell, where the *h*-BN is weakly bound to the substrate. These peculiar structures are reminiscent of "nanotents" with an ultimately thin "rainfly". Here we explore the implantation length (*i.e.*, the distance the atoms move before they come to rest as interstitial defects) and the thermal stability of these atomic agglomerates above room temperature. The results are obtained by variable-temperature scanning tunneling microscopy and density functional theory calculations.

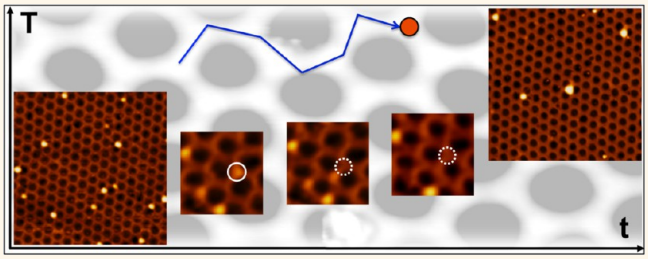

KEYWORDS: hexagonal boron nitride · graphene · implantation length · thermal stability · nanotent

Atomically thin layers of graphene[1] or hexagonal boron nitride (*h*-BN)[2] on metal surfaces have been extensively studied in recent years. These single layers consist of either carbon or boron nitride units and are studied in view of molecular self-assembly,[3−7] charge transfer,[8,9] or intercalation.[10−15] Importantly, such sp^2 monolayers that are formed by chemical vapor deposition (CVD) or segregation processes on a variety of substrates[3,9,11,16−20] exhibit superstructures with lattice constants up to a few nanometers.

For structuring or self-assembly processes on such monolayer systems, it is crucial to control the position of the atoms or molecules, ideally at room temperature. For this purpose, ion beam irradiation[21] has proven to be an efficient method, which can generate a variety of features, such as self-organization,[22] engineering of nanostructures,[23] quantum size effects,[24] magnetism in the graphene sheet,[25,26] site-selective etching,[27] or hillock formation, if highly charged ions are applied.[28] Recently, Standop *et al.* reported defect patterns on graphene/Ir(111) after ion beam bombardment.[29] By applying 5 keV Xe^+, they found that the ions are channeled between graphene and the Ir substrate, leading to chain formation of vacancy clusters. However, 5 keV Xe^+ ions may produce a variety of different structures. One approach to control this variety is to reduce the ion energy. For this purpose, low energy ions close to the penetration threshold (on the order of 100 eV) are better suited.

In previous work, we reported that Ar atoms may be immobilized beneath a single layer of *h*-BN on Rh(111) or graphene on Ru(0001), and highly regular holes with 2 nm diameter within the *h*-BN layer can be induced upon annealing, which are likely related to the vacancy defects from the penetration process.[30] It was found that the immobilization occurs at distinct sites beneath the "wire crossings" (WXA and WXB, for which we refer in this paper briefly as A and B sites) of the *h*-BN nanomesh superhoneycomb. Here, we show on the implantation length (*i.e.*, the distance that Ar atoms move after penetration through the *h*-BN monolayer before they come to rest in "nanotents") and on the thermal stability of these artificial structures. The occupation ratio between the two distinct sites A and B depends on the ion dose and the annealing temperature. The annealing

* Address correspondence to greber@physik.uzh.ch.

Received for review November 11, 2013 and accepted December 14, 2013.

Published online December 14, 2013
10.1021/nn405907a

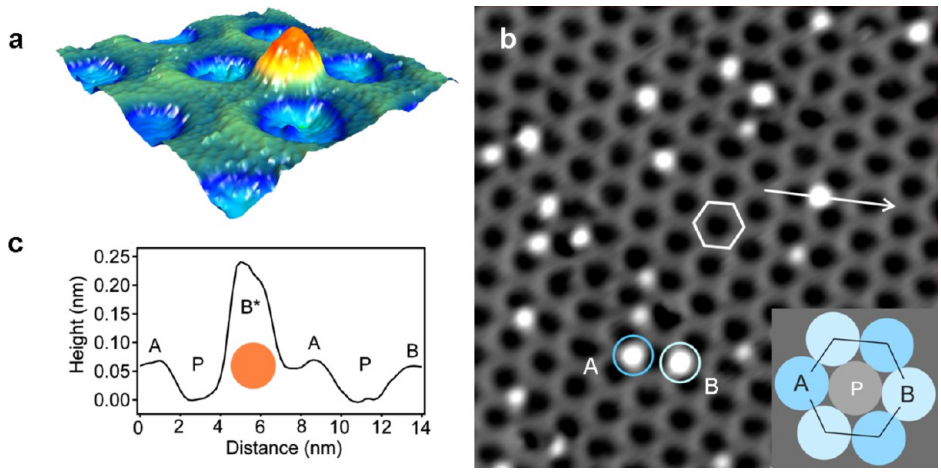

Figure 1. STM data of ion-implanted Ar beneath the *h*-BN/Rh(111) nanomesh at room temperature. (a) Three-dimensional STM image of one Ar nanotent (red-yellow peak). The green and blue regions represent wires and pores of the nanomesh, respectively. (b) STM image (38 × 38 nm^2) showing the selective Ar implantation: Ar locates at two distinct sites beneath nanomesh wire crossings (labeled as A (dark blue circle) and B (light blue circle)) but not in the pores (P). The bright protrusions are Ar clusters. The hexagon represents the honeycomb supercell, also shown in the bottom-right inset. $U_t = -1.10$ V, $I_t = 0.10$ nA. (c) Cross-sectional profile along the white line in panel b. A pore, an occupied B site, an empty A site, and another pore are indicated.

process increases the nanotent volume and indicates Ar clustering, where nanotents at A sites are more stable. Furthermore, we present data of Ar diffusion between *h*-BN and the Rh(111) substrate obtained by scanning tunneling microscopy (STM) at variable temperatures and density functional theory (DFT) calculations. These results are important for the understanding of the thermalization and diffusion, and will eventually allow further functionalization of sp^2 layer systems.

The *h*-BN nanomesh is a corrugated single layer of hexagonal boron nitride reminiscent of a honeycomb superstructure.[31] It forms by high-temperature CVD of borazine on the Rh(111) surface. The lattice constant of 3.2 nm is determined by the mismatch between the boron nitride and Rh. The unit cell of the *h*-BN nanomesh consists of 13 × 13 BN units on 12 × 12 Rh atoms. This appears as a mesh shape with "pores" of about 2 nm diameter and surrounding weakly bound "wire" regions with a larger *h*-BN distance to the substrate.[31,32]

RESULTS AND DISCUSSION

Figure 1 shows STM data after exposing the *h*-BN nanomesh to low energy Ar^+ ions. The ions penetrate the *h*-BN monolayer and stop below the *h*-BN layer but above the Rh(111) surface. They appear as bright protrusions with certain heights, such as the red-yellow peak in the three-dimensional (3D) view of implanted Ar beneath the *h*-BN monolayer in Figure 1a. The STM topography image in Figure 1b displays Ar protrusions at room temperature. These protrusions emerge after ion exposure and can be observed at positive and negative tunneling voltages. They are stable at room temperature and also survive exposure to air. Interestingly, the implantation process shows a pronounced selectivity: Ar atoms do not rest in pore sites (P) of the *h*-BN nanomesh but are situated beneath the wires, particularly where wires cross. Based on STM and DFT calculations of the atomic structure of the *h*-BN nanomesh on Rh(111),[31,33,34] the honeycomb superstructure exhibits two different wire crossing sites. They are given by the different registry to the Rh(111) substrate: one site with boron on top of a Rh atom and nitrogen at hexagonal close-packed (hcp) hollow sites (*i.e.*, B-top, N-hcp) and another one where boron stays at hcp hollow sites and nitrogen at face-centered cubic (fcc) sites, namely, (B-hcp, N-fcc). The different registries of *h*-BN on Rh are responsible for the modulation of the electronic properties, which is well-recognized by the modulation in brightness of the simulated STM topography.[32] This calculated result is consistent with experimental STM topography data of the nanomesh, which shows one wire crossing site to be slightly brighter (higher) than the other one (see Figure 1c).[30,31] The higher site (B-top, N-hcp) is labeled as A site (short for WXA, dark blue circle in Figure 1b), and the (B-hcp, N-fcc) site is named B site (short for WXB, light blue circle in Figure 1b). After ion exposure, A and B sites are populated with distinct probabilities, which depend on the ion beam parameters such as the ion dose, energy, impact angle, and the sample temperature. The hexagon imposed in Figure 1b represents the superhoneycomb unit cell of *h*-BN/Rh(111) with distinct regions that differ in registry, such as pores (P) and wires (A and B), which are displayed in the bottom-right inset. The image line profile in Figure 1c displays the height as measured from the bottom of the nanomesh pore along the white line in panel b. The cut passes through a pore, an Ar protrusion (nanotent) at a B site, an empty A site, and another pore of the nanomesh.

Figure 2 illustrates the correlation between the protrusion site ratio $N_B/N_A = \rho_{BA}$ of Ar nanotents and

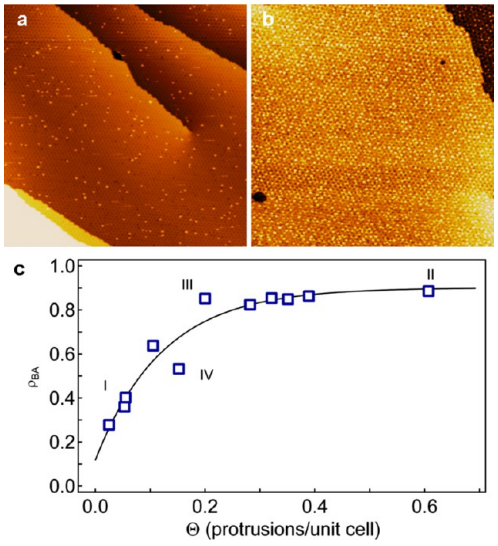

Figure 2. Adsorption site-selectivity modified by implanted Ar coverage at room temperature (RT). (a,b) Large-area RT-STM topography images (190 × 190 nm^2) at low (a, 0.06 Ar protrusions per nanomesh unit cell) and high (b, 0.61 protrusions per unit cell) coverage of implanted Ar beneath *h*-BN on Rh(111). (a) U_t = 1.00 V, I_t = 0.02 nA. (b) U_t = −1.10 V, I_t = 0.10 nA. The curve in c displays correlation between the N_B/N_A ratio ρ_{BA} and the initial nanotent coverage Θ at room temperature. Implanted Ar shows distinct selectivity at low coverage (the A site is favorable). The STM images in a and b are the data points I and II; III corresponds to data in ref 30; IV is the starting condition of the data in Figure 3.

the average number of nanotents per nanomesh unit cell (*i.e.*, coverage Θ). Figure 2a shows a room temperature large-area STM image at low Ar coverage after exposure to low energy Ar^+ ions corresponding to a sputter charge density of 4.4 × 10^{11} *e*/cm^2. One bright protrusion represents one nanotent housing one or more Ar atoms. We count 0.06 protrusions per 12 × 12 Rh unit cell, where 71 ± 7% of the protrusions are at A sites. The ratio is compared to a sample with higher nanotent density in Figure 2b. It displays 0.61 protrusions per nanomesh unit cell after exposure to a sputter charge density of 4.9 × 10^{12} *e*/cm^2. It shows 53 ± 3% of Ar nanotents at A sites. In order to investigate the relationship between the initial protrusion site ratio ρ_{BA} and the Ar coverage, a series of samples with different Ar exposures were prepared, and the corresponding N_B/N_A ratios ρ_{BA} were determined according to the room temperature STM data. Figure 2c demonstrates the coverage dependence of the initial protrusion ratio ρ_{BA} at room temperature. It contains significant information on the thermalization process during Ar implantation and clearly shows that ρ_{BA} increases with increasing Ar coverage. At low Ar ion exposure, the A site is favored, and most of the Ar atoms thermalize at A sites, as shown in Figure 2a and the data point I in Figure 2c. For higher Ar exposure, Ar also gradually populates B sites (Figure 2b and the data point II in Figure 2c). Our previously reported work with Ar nanotent coverage of 0.2 protrusions per unit cell is the data point marked with III in Figure 2c. Clearly, the plot of the ratio ρ_{BA} indicates that the selectivity of Ar atoms decreases at higher Ar exposure. When the Ar nanotent coverage increases, the ratio ρ_{BA} grows and approaches approximately 0.9 at the highest Ar doses applied. For Ar nanotent coverages between 1 and 2 protrusions per unit cell, the periodic structure of nanomesh gets lost.

The N_B/N_A ratio ρ_{BA} dependence on the coverage suggests that the Ar atoms do not stick at their impact site but move further beneath the surface before they come to rest at an A or at a B site. For the limit of zero coverage, when few Ar nanotents are distant and do not interact with each other, ρ_{BA} is minimal, which is in line with the theoretical picture that predicts interstitial vacancy formation energies of +2.7 and +3.5 eV with respect to a pristine nanomesh, respectively[30] (note that the energy values were incorrectly given as +2.6 and +3.7 eV in ref 30).

Empirically, the data in Figure 2c are fitted to a function

$$\rho_{BA}(\Theta) = \rho_0 + \alpha(1 - \exp(-\Theta/\Theta_c)) \qquad (1)$$

where we find a zero coverage limit ρ_0 of 0.12 ± 0.10, a factor α of 0.8 ± 0.1, and a critical coverage Θ_c of 0.12 ± 0.04; ρ_0 is related to the energy difference between singly occupied A and B sites ΔE_{BA} of 0.8 eV. Setting $\rho_0 = \exp(-\Delta E_{BA}/k_B T_{eff})$, we get from the Boltzmann factor an effective temperature T_{eff} on the order of 4400 K. Such hyperthermal energies are expected to have a significant impact on the resulting structures. The fact that α is larger than zero indicates that the interaction of an incoming Ar ion must also influence the already implanted atoms and lead to a redistribution of the nanotent locations. Θ_c contains information on the interaction cross section of the Ar atoms upon implantation, that is, a measure on how far the atoms move and interact in order to dissipate their energy after penetration of the *h*-BN layer. This cross section is reflected in the area σ_c to find a single protrusion at the critical coverage (σ_c = 1 protrusion/Θ_c = 8.3 nanomesh unit cells). From $\sqrt{\sigma_c}$, we get an "effective thermalization path length" between penetration and immobilization of about 8.6 nm. These considerations are reminiscent of the seminal work of Brune *et al.*, who reported surface migration of "hot" adatoms after O_2 dissociation on an Al(111) surface, where they could infer from the observation of the distance between single oxygen atoms an energy dissipation path length longer than 8 nm.[35] Our analysis for the present case is another confirmation on how strong the atomic friction can be, and that STM allows access to this kind of dynamics by observation of the impact patterns.

Figure 3 shows the thermal history of a sample with an initial coverage Θ of 0.15 protrusions per nanomesh supercell. The sample has been investigated during

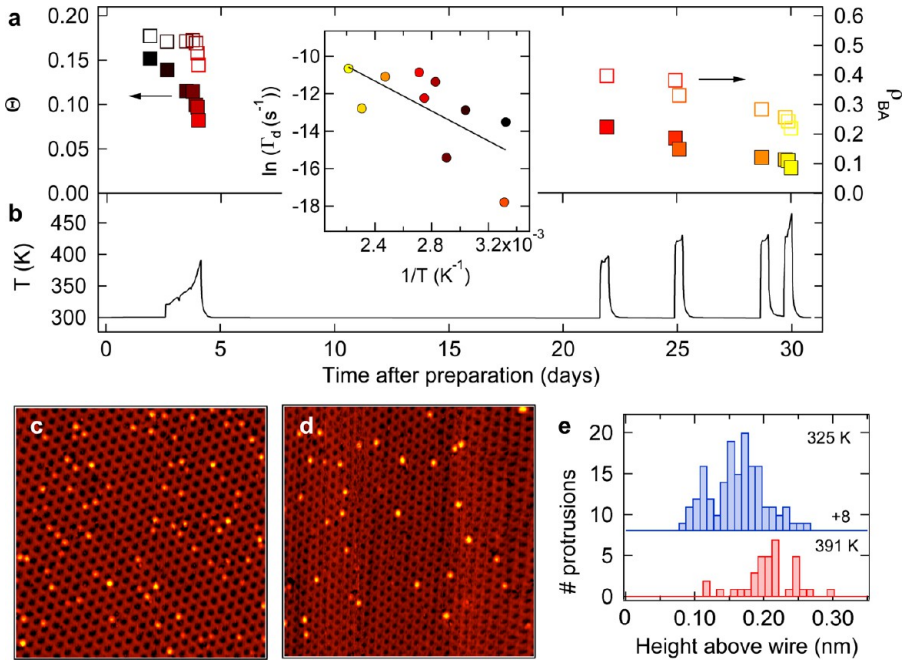

Figure 3. Long-term thermal history of a sample at temperatures between 300 and 460 K. (a) Evolution of an initial protrusion coverage Θ of 0.15 protrusions per unit cell (data point IV in Figure 2c). The coverage Θ (solid squares) and the N_B/N_A ratio ρ_{BA} (open squares) decrease with time and temperature. (b) Temperature history for the whole process. The inset shows the disappearance rate Γ_d of the Ar protrusions as a function of reciprocal temperature. The color code of the symbols corresponds to the time. (c,d) STM images (80 × 80 nm^2) measured at 325 and 391 K. The Ar protrusions decrease in number while they enlarge in size with increasing temperature. (c) $U_t = -1.10$ V, $I_t = 0.10$ nA. (d) $U_t = -1.10$ V, $I_t = 0.10$ nA. (e) Height distribution of the nanotents in c (blue) and d (red). The height is measured from the top of the wires of the *h*-BN nanomesh.

1 month with scanning tunneling microscopy at variable temperatures. Each data point represents an individual area of the sample surface since the thermal drift in our instrument does not allow for the tracing of an individual protrusion in a temperature window that exceeds $\Delta T = 15$ K. Clearly, the coverage (solid squares) decreases in parallel with a shift of ρ_{BA} (empty squares) with time and temperature. This indicates a redistribution driven by a thermally activated process (Figure 3a). In order to estimate an activation energy E_a and a prefactor ν, we apply first-order kinetics

$$dN = -N\nu\exp(-E_a/k_BT)dt \qquad (2)$$

where dN of N protrusions disappear in the time interval dt. $N(t)$ is the number of protrusions at time t, E_a is the activation energy, and ν is the attempt frequency. Evaluation of the disappearence rates $\Gamma_d = \nu\exp(-E_a/k_BT)$ in Figure 3a results in $E_a = 0.28 \pm 0.13$ eV and an attempt frequency range ν of $0.2 \times 10^{\pm 2}$ s^{-1}, with an anticorrelation between the $\ln(\Gamma_d)$ and the $1/T$ values of -0.67. First of all, this confirms the stability of the immobilized Ar atoms at room temperature, where we find for a given protrusion a disappearance rate below 1/8 per day. Furthermore, the low attempt frequency indicates that the kinetics cannot be described with a single elementary process that involves the activation of a single atom, where the attempt frequencies are on the order of molecular vibration periods of 10^{-13} s^{-1}.[36] The rearrangement of the Ar nanotents is thus a complicated kinetic process because many different elementary processes may occur at the same time and superimpose in the overall picture that is obtained by counting and assigning the protrusion density and ρ_{BA} as a function of temperature and time. However, the decrease of ρ_{BA} confirms again higher stability of A sites, as it was found for single atom protrusions by density functional theory.[30]

Observing a decrease of the number of nanotents, we have to address the question on where the Ar goes. Figure 3c,d show STM images recorded at 325 and 391 K for the same sample with initial Ar coverage Θ of 0.15 protrusions per unit cell (data point IV in Figure 2c). The number of Ar protrusions decreases, while the height (or the volume) of the protrusions gets significantly larger with increasing temperature (Figure 3e). According to the calculations of implantation energy of individual Ar atoms and Ar clusters,[30] the implantation energy cost per Ar atom decreases with increasing cluster size, which predicts Ar to cluster in the nanotents. The cluster size is determined by the Ar exposure and the annealing temperature. The more Ar that is trapped within a protrusion, the higher the protrusion gets. Figure 3e confirms Ar clustering, where between 325 and 391 K the average Ar protrusion height (here measured from the top of the wires) increases from

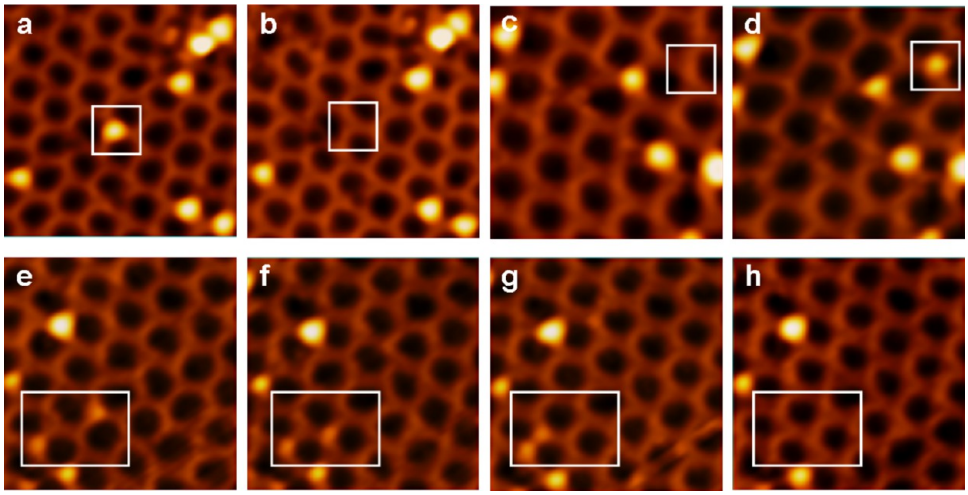

Figure 4. Three "hopping" events as observed on the *h*-BN/Ar/Rh(111) surface between 300 and 391 K. (a−h) Taken during continuously scanning under same scanning conditions: $U_t = -1.10$ V, $I_t = 0.10$ nA. Panels a and b show the disappearance of an Ar nanotent at a B site with height of 0.17 nm at 363 K (marked as a white square): 20 × 20 nm^2. The time interval of a and b is 75 s. (c,d) Appearance of an Ar nanotent at A site with a height of 0.14 nm at 337 K (white square): 16 × 16 nm^2. The time interval between c and d is 75 s. (e−h) Hopping of an Ar nanotent at a B site and disappearance of a nanotent at an A site, both with height of 0.08 nm at 363 K (white rectangle). The nanotent at the B site hops to an adjacent A site and then hops further to another B site until it disappears, while the nanotent at the A site stays at the same position until it disappears: 20 × 20 nm^2. The time intervals between e and f, f and g, and g and h are 300, 450, and 1350 s, respectively.

0.17 to 0.21 nm. This is in line with the picture that the Ar atoms of the disappearing protrusions join other nanotents and is further supported by X-ray photoelectron spectroscopy (XPS) that indicated no Ar 2p signal decreases upon annealing to 900 K.[30]

The kinetics shown in Figure 3a signal no simple diffusion behavior that would correspond to the hopping of individual Ar atoms with a single diffusion barrier. This makes the observation of Ar diffusion difficult. However, we have been able to observe three different classes of events of individual Ar protrusions: disappearance (see Figure 4a,b), appearance (Figure 4c,d), and hopping from one site to another (Figure 4e−h). Careful investigations have been carried out on the same sample. The temperature was ramped up slow enough to carry out simultaneous *in situ* STM measurements. The different kinds of events occur on the surface in the temperature window between 300 and 391 K. Out of all events, the most prominent effect is the disappearance of protrusions, which corresponds to more than 50% of all registered events. A similar phenomenon had been observed for the graphene/Xe/iridium system.[29] In that case, the effect was assigned to the melting of Ir clusters, that is, bright protrusions produced by 5 keV Xe^+ scattering on graphene/iridium. However, the fact that the second most prominent event is the appearance of protrusions (30%), as shown in Figure 4c,d, excludes a model of melting Rh clusters for our system. Besides the proof that the protrusions are caused by a foreign species (Ar^+),[30] the appearance of protrusions is a complex process; in particular, we cannot exclude that the protrusions appear from outside of the scan area. Finally, the hopping from one wire crossing site to another along the nanomesh is observed only for the smallest protrusions based on a series of *in situ* variable-temperature (VT) STM data, as shown in four frames in Figure 4e−h. Obviously, the height of "hopping" Ar protrusions is smaller than the normal surrounded Ar protrusions (0.08 and 0.14 nm, respectively).

Figure 5 summarizes the DFT results for the diffusion of a single Ar atom between an A and an adjacent B site and the energies of two Ar atoms at one or two A and/or B sites (see Table 1). The diffusion path has been calculated using the nudged elastic band method,[37] where 48 configurations have been evenly distributed between the A and B stable states. Figure 5a is a 3D view of the average coordinates of the 48 calculated beads, where it appears how the Ar atom has to "dig" a "tunnel" in order to diffuse, by displacing outward the closest BN pairs. A sketch of an extended path is shown in Figure 5b, where the coordinates of the nanomesh supercell have been projected onto the surface and the path followed by the Ar atoms is shown as a thick line. The color of the line refers to the energy of the corresponding configuration (Figure 5c). It is observed that the diffusion path meanders *via* boron at top sites between A and B. Figure 5c displays the energy of a single Ar atom on the diffusion path between an A and a B site in the superhoneycomb. The calculations give an energy difference between the two sites of 0.8 eV. This difference is mainly due to the different coordination of the *h*-BN with respect to the boron and metal sites, which favors the (B-top, N-hcp) coordination of the A sites above the (B-hcp, N-fcc) coordination of the B sites. The fact that the confined Ar likes to coordinate to the boron atoms, with lower electron density, is confirmed also by the choice of intermediate sites along

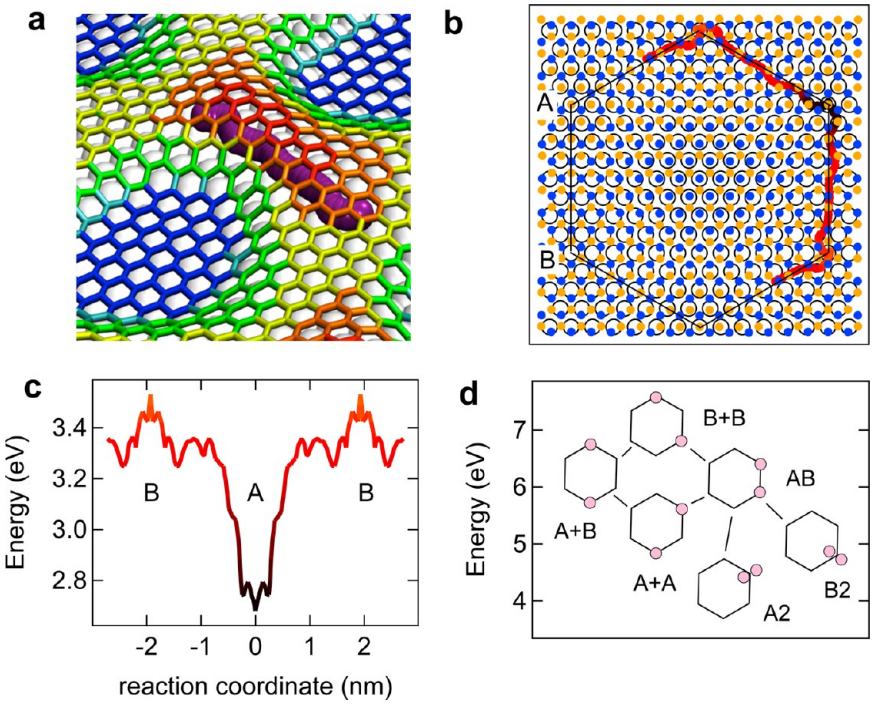

Figure 5. Calculated potential energies for one and two implanted Ar atoms. (a) Three-dimensional view of the average of the atom coordinates of an Ar atom diffusing between an A and a B site. The color coding of the nanomesh mimics the color code in Figure 1a. (b) Lateral coordinates of the boron (orange dots), nitrogen (blue dots), and rhodium (black circles) in the nanomesh superhoneycomb. The black to red line indicates the diffusion path between A and B. (c) Ar energy along the path shown in b. One Ar atom is most stable at an A site. (d) Diffusion energy tree for processes involving two Ar atoms at A and/or B sites. The configurations of B+B, A+B, A+A, AB, B2, and A2 are indicated by the pictograms. The energies are given in Table 1. Possible single hopping pathways are indicated with lines.

TABLE 1. Calculated Formation Energies of Different Nanotent Configurations with One and/or Two Ar Atoms at A and/or B Interstitial Sites, Relative to the *h*-BN Nanomesh and Free Ar Atoms in eV[a]

B+B	A+B	A+A	AB	B2	A2
7.06	6.21	5.36	6.14	5.05	4.21

[a] The B+B, A+B, and A+A configurations are the sum of two single nanotents. AB is the energy of two neighboring nanotents in the same unit cell. B2 and A2 are the most favorable doubly occupied tents.

the path. The lowest energies are always associated with sites beneath boron atoms. On the other hand, the highest transition state corresponds to a site where Ar is beneath a nitrogen atom. Moreover, the calculations show that a single Ar atom is metastable at B site but "protected" by several low energy barriers on the way from B to A. These barriers are on the order of 100 meV, and thus much smaller than the global barrier value of about 300 meV obtained from the data in Figure 3. We therefore propose that the thermal processes that we observe above room temperature are mainly due to Ar cluster rearrangements, involving more than one atom. Figure 5d supports this picture. It shows the energy hierarchy of two argon atoms in one or two different nanotents. These six configurations are labeled as B+B, A+B, A+A, AB, B2, and A2, where B+B labels two nanotents at two noninteracting B sites housing one Ar atom each, *etc*. This diagram is instructive and shows that A2 is most stable and requires an activation energy of 1.93 eV in order to dissociate into AB. This AB state must also be reached for B2 and possibly A+A in order to obtain Ar hopping. The activation energies for these two processes are 1.09 and 0.85 eV, which also demonstrates the higher stability of B2 as compared to A+B. It is interesting to note that the calculations also indicate an attractive interaction between two neighboring single nanotents since the AB energy is 0.07 eV lower than that of two noninteracting protrusions A+B.

For higher numbers of Ar atoms, the diffusion tree as shown in Figure 5d becomes more complex, though the basic idea remains, that is, the preference for clustering at A sites.

CONCLUSIONS

In conclusion, the specific site-selectivity, implantation length, and thermal stability of single atoms immobilized beneath a 3.2 nm honeycomb superstructure of a boron nitride single layer on an Rh substrate is reported. The adsorption site-selectivity can be controlled by the ion exposure and the sample temperature. At low coverage, Ar implantation shows distinct selectivity. *In situ* variable-temperature measurements reveal that Ar nanotents decrease in

number while growing in size significantly upon annealing treatment, even though the total amount of Ar remains the same. The reported effect provides a way to modify and use the ultimately thin membrane on surfaces, such as specific site-doping for a sp^2 monolayer.

METHODS

Experimental. The experiments were performed in an ultrahigh vacuum (UHV) system with a base pressure of 1×10^{-10} mbar with a variable-temperature scanning tunneling microscope (Omicron VT-STM). The *h*-BN nanomesh samples were produced with the standard recipe.[16] The ion implantation was achieved with a Specs IQP 10/35 Penning-type ion source run at lowest acceleration potential. The sputter charge density corresponds to the integrated sputter current density. The STM measurements were carried out with electrochemically etched tungsten tips. All STM images were taken in constant-current mode.

Theory. Calculations are performed using Kohn–Sham DFT within the GPW formalism as implemented in the Quickstep module in the CP2K program package.[38] Dual-space pseudopotentials[39] are used to describe the interaction of valence electrons with atomic cores. The pseudopotentials for boron and nitrogen assume 3 and 5 valence electrons, respectively. The atomic cores of the Rh are described by potentials with 9 valence electrons. The Gaussian basis sets chosen for this type of application are of the molecularly optimized type.[40] The PW energy cutoff for the expansion of the density is set at 500 Ry. The Brillouin zone is sampled only at the Γ point. Exchange and correlation are calculated with the revised Perdew–Burke–Ernzerhof (PBE)[41] GGA exchange-correlation (XC) functional. Long-range dispersion interactions have been computed using DFT-D3 formalisms.[42]

We employ a slab-like model where the simulation cell consists of four layers of 12×12 Rh(111) units terminated on one side by a 13×13 *h*-BN overlayer. Periodic boundary conditions are applied, and interactions with periodic images in the direction perpendicular to the exposed surface are avoided by adding about 20 Å of vacuum space above the slab. The atoms at the bottom Rh layer are kept fixed in the bulk positions. This computational setup has been already successfully applied for several previous studies related to *h*-BN/Rh-(111).[32,43] The diffusion path has been calculated using the climbing image nudged elastic band method.[37] The initial path consists of 48 configurations between A and B generated by linear interpolation of the coordinates. The band beads have been evenly distributed moving from A to B along the *y* axis. The optimization of the path has been performed until the atomic forces over the whole path were below 0.005 au/Å.

Conflict of Interest: The authors declare no competing financial interest.

Acknowledgment. Financial support by the Swiss National Science Foundation is gratefully acknowledged. The Swiss National Supercomputer Centre (CSCS) is acknowledged for the generous allocation of computer time.

REFERENCES AND NOTES

1. Batzill, M. The Surface Science of Graphene: Metal Interfaces, CVD Synthesis, Nanoribbons, Chemical Modifications, and Defects. *Surf. Sci. Rep.* **2012**, *67*, 83–115.
2. Goriachko, A.; Over, H. Modern Nanotemplates Based on Graphene and Single Layer *h*-BN. *Int. J. Res. Phys. Chem. Chem. Phys.* **2009**, *223*, 157–168.
3. N'Diaye, A. T.; Bleikamp, S.; Feibelman, P. J.; Michely, T. Two-Dimensional Ir Cluster Lattice on a Graphene Moire on Ir(111). *Phys. Rev. Lett.* **2006**, *97*, 215501.
4. Dil, H.; Lobo-Checa, J.; Laskowski, R.; Blaha, P.; Berner, S.; Osterwalder, J.; Greber, T. Surface Trapping of Atoms and Molecules with Dipole Rings. *Science* **2008**, *319*, 1824–1826.
5. Mao, J. H.; Zhang, H. G.; Jiang, Y. H.; Pan, Y.; Gao, M.; Xiao, W. D.; Gao, H. J. Tunability of Supramolecular Kagome Lattices of Magnetic Phthalocyanines Using Graphene-Based Moire Patterns as Templates. *J. Am. Chem. Soc.* **2009**, *131*, 14136.
6. Pollard, A. J.; Perkins, E. W.; Smith, N. A.; Saywell, A.; Goretzki, G.; Phillips, A. G.; Argent, S. P.; Sachdev, H.; Muller, F.; Hufner, S.; *et al.* Supramolecular Assemblies Formed on an Epitaxial Graphene Superstructure. *Angew. Chem., Int. Ed.* **2010**, *49*, 1794–1799.
7. Ma, H. F.; Ding, Y.; Iannuzzi, M.; Brugger, T.; Berner, S.; Hutter, J.; Osterwalder, J.; Greber, T. Chiral Distortion of Confined Ice Oligomers (*n*=5,6). *Langmuir* **2012**, *28*, 15246–15250.
8. Tseng, T.; Urban, C.; Wang, Y.; Otero, R.; Tait, S. L.; Alcamí, M.; Écija, D.; Trelka, M.; Gallego, J. M.; Lin, N.; *et al.* Charge-Transfer-Induced Structural Rearrangements at both Sides of Organic/Metal Interfaces. *Nat. Chem.* **2010**, *2*, 374–379.
9. Coletti, C.; Riedl, C.; Lee, D. S.; Krauss, B.; Patthey, L.; Klitzing, K.; Smet, J. H.; Starke, U. Charge Neutrality and Band-Gap Tuning of Epitaxial Graphene on SiC by Molecular Doping. *Phys. Rev. B* **2010**, *81*, 235401.
10. Auwärter, W.; Muntwiler, M.; Greber, T.; Osterwalder, J. Co on h-BN/Ni(111): From Island to Island-Chain Formation and Co Intercalation. *Surf. Sci.* **2002**, *511*, 379–386.
11. Sutter, P. W.; Flege, J.-I.; Sutter, E. A. Epitaxial Graphene on Ruthenium. *Nat. Mater.* **2008**, *7*, 406–411.
12. Preobrajenski, A. B.; Ng, M. L.; Vinogradov, N. A.; Vinogradov, A. S.; Lundgren, E.; Mikkelsen, A.; Martensson, N. Impact of Oxygen Coadsorption on Intercalation of Cobalt under the h-BN Nanomesh. *Nano Lett.* **2009**, *9*, 2780–2787.
13. Riedl, C.; Coletti, C.; Iwasaki, T.; Zakharov, A. A.; Starke, U. Quasi-Free-Standing Epitaxial Graphene on SiC Obtained by Hydrogen Intercalation. *Phys. Rev. Lett.* **2009**, *103*, 246804.
14. Brugger, T.; Ma, H.; Iannuzzi, M.; Berner, S.; Winkler, A.; Hutter, J.; Osterwalder, J.; Greber, T. Nanotexture Switching of Single-Layer Hexagonal Boron Nitride on Rhodium by Intercalation of Hydrogen Atoms. *Angew. Chem., Int. Ed.* **2010**, *49*, 6120–6124.
15. Mao, J. H.; Huang, L.; Pan, Y.; Gao, M.; He, J. F.; Zhou, H. T.; Guo, H. M.; Tian, Y.; Zou, Q.; Zhang, L. Z.; *et al.* Silicon Layer Intercalation of Centimeter-Scale, Epitaxially Grown Monolayer Graphene on Ru(0001). *Appl. Phys. Lett.* **2012**, *100*, 093101.
16. Corso, M.; Auwärter, W.; Muntwiler, M.; Tamai, A.; Greber, T.; Osterwalder, J. Boron Nitride Nanomesh. *Science* **2004**, *303*, 217–220.
17. Sutter, P.; Sadowski, J. T.; Sutter, E. Graphene on Pt(111): Growth and Substrate Interaction. *Phys. Rev. B* **2009**, *80*, 245411.
18. Brugger, T.; Günther, S.; Wang, B.; Dil, J. H.; Bocquet, M.-L.; Osterwalder, J.; Wintterlin, J.; Greber, T. Comparison of Electronic Structure and Template Function of Single-Layer Graphene and a Hexagonal Boron Nitride Nanomesh on Ru(0001). *Phys. Rev. B* **2009**, *79*, 045407.
19. Li, X. S.; Cai, W. W.; An, J.; Kim, S.; Nah, J.; Yang, D. X.; Piner, R.; Velamakanni, A.; Jung, I.; Tutuc, E.; *et al.* Large-Area Synthesis of High-Quality and Uniform Graphene Films on Copper Foils. *Science* **2009**, *324*, 1312–1314.
20. Joshi, S.; Ecija, D.; Koitz, R.; Iannuzzi, M.; Seitsonen, A. P.; Hutter, J.; Sachdev, R.; Vijayaraghavan, S.; Bischoff, F.; Seufert, K.; *et al.* Boron Nitride on Cu(111): An Electronically Corrugated Monolayer. *Nano Lett.* **2012**, *12*, 5821–5828.
21. Chan, W. L.; Chason, E. Making Waves: Kinetic Processes Controlling Surface Evolution during Low Energy Ion Sputtering. *J. Appl. Phys.* **2007**, *101*, 121301.
22. Facsko, S.; Dekorsy, T.; Koerdt, C.; Trappe, C.; Kurz, H.; Vogt, A.; Hartnagel, H. L. Formation of Ordered Nanoscale

Semiconductor Dots by Ion Sputtering. *Science* **1999**, *285*, 1551–1553.
23. Krasheninnikov, A. V.; Banhart, F. Engineering of Nanostructured Carbon Materials with Electron or Ion Beams. *Nat. Mater.* **2007**, *6*, 723–733.
24. Schmid, M.; Hebenstreit, W.; Varga, P.; Crampin, S. Quantum Wells and Electron Interference Phenomena in Al Due to Subsurface Noble Gas Bubbles. *Phys. Rev. Lett.* **1996**, *76*, 2298–2301.
25. Ugeda, M. M.; Brihuega, I.; Guinea, F.; Gómez-Rodríguez, J. M. Missing Atom as a Source of Carbon Magnetism. *Phys. Rev. Lett.* **2010**, *104*, 096804.
26. Ugeda, M. M.; Fernández-Torre, D.; Brihuega, I.; Pou, P.; Martínez-Galera, A. J.; Pérez, R.; Gómez-Rodríguez, J. M. Point Defects on Graphene on Metals. *Phys. Rev. Lett.* **2011**, *107*, 116803.
27. Broekmann, P.; Mewe, A.; Wormeester, H.; Poelsema, B. Step Edge Selection during Ion Erosion of Cu(001). *Phys. Rev. Lett.* **2002**, *89*, 146102.
28. Aumayr, F.; Facsko, S.; El-Said, A. S.; Trautmann, C.; Schleberger, M. Single Ion Induced Surface Nanostructures: A Comparison between Slow Highly Charged and Swift Heavy Ions. *J. Phys.: Condens. Matter* **2011**, *23*, 393001.
29. Standop, S.; Lehtinen, O.; Herbig, C.; Lewes-Malandrakis, G.; Craes, F.; Kotakoski, J.; Michely, T.; Krasheninnikov, A.; Busse, C. Ion Impacts on Graphene/Ir(111): Interface Channeling, Vacancy Funnels, and a Nanomesh. *Nano Lett.* **2013**, *13*, 1948–1955.
30. Cun, H.; Iannuzzi, M.; Hemmi, A.; Roth, S.; Osterwalder, J.; Greber, T. Immobilizing Individual Atoms beneath a Corrugated Single Layer of Boron Nitride. *Nano Lett.* **2013**, *13*, 2098–2103.
31. Berner, S.; Corso, M.; Widmer, R.; Groening, O.; Laskowski, R.; Blaha, P.; Schwarz, K.; Goriachko, A.; Over, H.; Gsell, S.; *et al.* Boron Nitride Nanomesh: Functionality from a Corrugated Monolayer. *Angew. Chem., Int. Ed.* **2007**, *46*, 5115–5119.
32. Díaz, J. G.; Ding, Y.; Koitz, R.; Seitsonen, A. P.; Iannuzzi, M.; Hutter, J. Hexagonal Boron Nitride on Transition Metal Surfaces. *Theor. Chem. Acc.* **2013**, *132*, 1350–1366.
33. Goriachko, A.; He, Y.; Knapp, M.; Over, H.; Corso, M.; Brugger, T.; Berner, S.; Osterwalder, J.; Greber, T. Self-Assembly of a Hexagonal Boron Nitride Nanomesh on Ru(0001). *Langmuir* **2007**, *23*, 2928–2931.
34. Laskowski, R.; Blaha, P. Unraveling the Structure of the h-BN/Rh(111) Nanomesh with *Ab Initio* Calculations. *J. Phys.: Condens. Matter.* **2008**, *20*, 064207.
35. Brune, H.; Wintterlin, J.; Behm, R. J.; Ertl, G. Surface Migration of "Hot" Adatoms in the Course of Dissociative Chemisorption of Oxygen on Al(111). *Phys. Rev. Lett.* **1992**, *68*, 624–626.
36. King, D. A. Thermal Desorption from Metal Surfaces: A Review. *Surf. Sci.* **1975**, *47*, 384–402.
37. Henkelman, G.; Jonsson, H. Improved Tangent Estimate in the Nudged Elastic Band Method for Finding Minimum Energy Paths and Saddle Points. *J. Chem. Phys.* **2000**, *113*, 9978–9985.
38. CP2k Developers Group under the Terms of the GNU General Public Licence; see http://www.cp2k.org, 2012.
39. Goedecker, S.; Teter, M.; Hutter, J. Separable Dual-Space Gaussian Pseudopotentials. *Phys. Rev. B* **1996**, *54*, 1703–1710.
40. VandeVondele, J.; Hutter, J. Gaussian Basis Sets for Accurate Calculations on Molecular Systems in Gas and Condensed Phases. *J. Chem. Phys.* **2007**, *127*, 114105.
41. Zhang, Y.; Yang, W. Generalized Gradient Approximation Made Simple. *Phys. Rev. Lett.* **1998**, *80*, 890–891.
42. Grimme, S.; Antony, J.; Ehrlich, S.; Krieg, H. A Consistent and Accurate *Ab Initio* Parametrization of Density Functional Dispersion Correction (DFT-D) for the 94 Elements H-Pu. *J. Chem. Phys.* **2010**, *132*, 154104.
43. Ding, Y.; Iannuzzi, M.; Hutter, J. Investigation of Boron Nitride Nanomesh Interacting with Water. *J. Phys. Chem. C* **2011**, *115*, 13685–13692.